

Stimulated Raman Scattering Simulation for Imaging Optimization

Liron Zada (✉ lironzada@gmail.com)

Vrije Universiteit Amsterdam <https://orcid.org/0000-0002-8419-1945>

Bart Fokker

Vrije Universiteit Amsterdam

Heather A. Leslie

Vrije Universiteit Amsterdam

A. Dick Vethaak

Vrije Universiteit Amsterdam

Johannes F. de Boer

Vrije Universiteit Amsterdam

Freek Ariese

Vrije Universiteit Amsterdam

Research

Keywords: Raman, Simulation, Imaging, Optimization, Resolution, Microscopy, Non-linear, Multiplex, Lock-in amplifier, Modulation

Posted Date: November 18th, 2020

DOI: <https://doi.org/10.21203/rs.3.rs-99940/v1>

License:  This work is licensed under a Creative Commons Attribution 4.0 International License.

[Read Full License](#)

Version of Record: A version of this preprint was published at Journal of the European Optical Society-Rapid Publications on June 16th, 2021. See the published version at <https://doi.org/10.1186/s41476-021-00155-w>.

1 Stimulated Raman scattering simulation for imaging 2 optimization

3 Liron Zada^{1,2}, Bart Fokker¹, Heather A. Leslie², A. Dick Vethaak^{2,3}, Johannes F. de Boer¹, Freek
4 Ariese^{1*}

5 Affiliations:

6 ¹LaserLab Amsterdam, Department of Physics and Astronomy, Faculty of Sciences Vrije
7 Universiteit Amsterdam, De Boelelaan 1081, 1081 HV Amsterdam, The Netherlands.

8 ²Department of Environment and Health, Vrije Universiteit Amsterdam, De Boelelaan 1085,
9 1081 HV Amsterdam, The Netherlands.

10 ³Deltares, Marine and Coastal Systems, P.O. Box 177, 2600 MH Delft, The Netherlands.

11 *Correspondence:

12 Liron Zada

13 LaserlaB Amsterdam, Department of Physics and Astronomy, Faculty of Sciences Vrije
14 Universiteit Amsterdam, De Boelelaan 1081, 1081 HV Amsterdam, The Netherlands

15 Telephone number: +31 20 59 85425

16 Email: lironzada@gmail.com

17 **Abstract**

18 Two simulation programs of a stimulated Raman scattering microscopy (SRS) imaging system
19 with lock-in amplifier (LIA) detection were developed. SRS is an imaging technique based on
20 the vibrational Raman cross-section as the contrast mechanism and enables fast, label-free
21 imaging. Most SRS implementations are based on a LIA detection of a modulated signal.
22 However, building and operating such SRS set-ups still poses a challenge when selecting the
23 LIA parameter settings for optimized acquisition speed or image quality. Moreover, the type of
24 sample, e.g. a sparse sample vs. a densely packed sample, the required resolution as well as the
25 Raman cross-section and the laser powers affect the parameter choice.

26 A simulation program was used to find these optimal parameters. The focal spot diameters of
27 the individual lasers (pump and Stokes) were used to estimate the effective SRS signal focal spot
28 and the (optical) spatial resolution. By calibrating the signal and noise propagation through an
29 SRS system for a known molecule, we estimated the signal and noise input to the LIA. We used
30 a low pass filter model to simulate the LIA behavior in order to find the optimal parameters (i.e.
31 filter order and time constant).

32 Optimization was done for either image quality (expressed as contrast to noise ratio) or
33 acquisition time. The targeted object size was first determined as a measure for the required
34 resolution. The simulation output consisted of the LIA parameters, pixel dwell time and contrast
35 to noise ratio.

36 In a second simulation we evaluated SRS imaging based on the same principles as the optimal
37 setting simulation, i.e. the signals were propagated through an imaging system and LIA

38 detection. The simulated images were compared to experimental SRS images of polystyrene
39 beads.

40 Finally, the same software was used to simulate multiplexed SRS imaging. In this study we
41 modeled a six-channel frequency-encoded multiplexed SRS system demodulated with six LIA
42 channels. We evaluated the inter-channel crosstalk as a function of chosen LIA parameters,
43 which in multiplex SRS imaging also needs to be considered.

44 These programs to optimize the contrast to noise ratio, acquisition speed, resolution and
45 crosstalk will be useful for operating stimulated Raman scattering imaging setup, as well as for
46 designing novel setups.

47 **Key words:**

48 Raman, Simulation, Imaging, Optimization, Resolution, Microscopy, Non-linear, Multiplex,
49 Lock-in amplifier, Modulation.

50 **Introduction**

51 Stimulated Raman scattering microscopy (SRS) is a non-linear imaging modality with a
52 spectral response similar to spontaneous Raman scattering. Compared with spontaneous Raman,
53 SRS offers an increase in mapping speed of several orders of magnitude. Unlike spontaneous
54 Raman, SRS is not affected by background fluorescence. SRS is realized by two laser beams that
55 directly probe a specific vibrational state of a molecule if their photon energy difference matches
56 the energy of a vibrational transition. Then the SRS signal can be detected as a gain in intensity
57 of the low energy beam (stimulated Raman gain of Stokes) and a loss in the high energy beam
58 intensity (stimulated Raman loss of pump)¹.

59 SRS, as a fast imaging modality, was first demonstrated by Freudiger et al.² and others^{3,4} with
60 the introduction of an amplitude modulation of one of the laser beams and demodulation by a
61 lock-in amplifier (LIA) for detection and noise filtering. Modulation at high frequency allowed
62 the rejection of the lasers' relative intensity noise (RIN) which dominates at frequencies below 1
63 MHz. A combination of a high modulation frequency, where the laser noise is low, and laser
64 powers at which the shot-noise surpasses the thermal noise, results in shot-noise limited
65 detection. After the probe beam is detected (e.g. the pump beam in stimulated Raman loss),
66 demodulation of the signal takes place by means of a LIA or alternatively home built electronics
67 (e.g. tuned amplifier⁵). Throughout this paper, we choose not to use the common convention of
68 Stokes and pump beams to keep the discussion general. Instead, we refer to the amplitude
69 modulated beam as the *carrier*, as it carries the amplitude modulation, and to the detected beam
70 as *probe*.

71 While the modulation frequency is mentioned as an important parameter in most studies, only a
72 few studies⁵⁻⁷ discussed the (low pass) filter bandwidth, which is an important parameter that
73 affects the acquisition speed and noise. Specifically for the LIA in the context of SRS, to the best
74 of our knowledge no in-depth analysis has been reported for the input parameters of the filter
75 bandwidth. While most SRS studies mention the time constant (TC), almost none⁸ mention the
76 equally important filter-order (n), which makes it impossible to calculate the bandwidth or
77 compare modalities reported in the literature. Since the conventional imaging manner of non-
78 linear modalities, such as SRS, is scanning the focal spot across the sample, the scanning speed,
79 the filter response, the focal spot size, and the spatial resolution in the scanning direction are
80 related. Thus, for an object of a given size and with the theory of the LIA filter response for a
81 given bandwidth, one can extract the optimal settings needed for imaging this object with SRS,

82 either with regard to the signal to noise ratio (SNR), contrast to noise ratio (CNR)⁹⁻¹¹ or to the
83 acquisition speed.

84 Here, we describe the operation principle of LIAs, and investigate the signal and noise
85 propagation in the time and frequency domain. Then, we link this to the physical properties of an
86 SRS setup, such as laser powers, focal spot size and pixel dwell time (PDT), in order to optimize
87 the SRS imaging. The optimization procedure is compiled into a simulation program in order to
88 address different imaging scenarios: optimization for CNR or imaging time in a sparse or tightly
89 packed sample. The rationale for the optimization for CNR, rather than SNR, is explained in the
90 optimal settings simulation part in the results section. A detailed description of the input and
91 output parameters of the software's user interface is given in the optimal settings simulation
92 section and in the supplementary material.

93 Furthermore, we generalize this result in order to demonstrate extended capabilities of this
94 analysis. An additional simulation with a visual output (called imaging simulation) was created,
95 based on the same LIA theory and input parameters. This simulation provides a qualitative image
96 visualization, either for narrowband SRS, or for a multiplex SRS setup that has multiple
97 modulated bands and multiple detection channels. As a test case, we analyze a simulated
98 frequency channel encoded multiplex SRS setup as demonstrated before^{12,13}, however in our
99 simulation the signal is demodulated with a multi-channel LIA. Here, crosstalk between channels
100 is also treated, in addition to resolution, CNR and acquisition speed.

101 **Theory: parameters of the lock-in amplifier**

102 The SRS signal is a small modulation carried on a large background. This large DC background
103 is the source for the laser RIN and shot noise. In the LIA this large DC background is filtered

104 out, and the small modulation is mixed with a reference frequency. Then, the signal amplitude is
 105 recovered by applying a low-pass filter, here modeled as a discrete time RC filter, which is an
 106 exponential running average filter¹⁴:

$$107 \quad (1) \quad X_{out}[k, T_s] = e^{-T_s/TC} X_{out}[k-1, T_s] + (1 - e^{-T_s/TC}) X_{in}[k, T_s]$$

108 Where k is the index of the processed sample X_{out} at specified discrete sampling times T_s . Thus,
 109 every X_{out} is a weighted averaged between the new input X_{in} and the previous sample X_{out} of $k-1$.
 110 It is possible to cascade these filters such that the signal and noise pass through multiple filters.
 111 The number of filters is called the filter order (n). The frequency domain response of the filter
 112 with TC and n is described as:

$$113 \quad (2) \quad H_n(\Delta f) = \frac{1}{(1+i 2\pi \Delta f TC)^n}$$

114 Where Δf is the difference between modulation frequency and the detection frequencies; the
 115 input frequencies to the LIA. The filter transmission which describes the signal propagation
 116 through such a filter is then:

$$117 \quad (3) \quad |H_n(\Delta f)| = \sqrt{\frac{1}{(1+(2\pi \Delta f TC)^2)^n}}$$

118 Measurements that verify this model in the frequency and time domain are provided in Figure
 119 S1 in the supporting information.

120 The possible noise sources in SRS are the thermal (Johnson–Nyquist) noise from the different
 121 electronic components, the shot noise from the detected (probe) laser light and the frequency
 122 dependent RIN¹⁵ from the laser source of the probe light. While the thermal noise is independent
 123 of the probe power, the shot noise is proportional to the square-root of the probe power. We
 124 ignored the RIN in our analysis for two reasons. One was the assumption that thermal or shot

125 noise limited systems cover most scenarios for SRS imaging, and provides a sufficient
126 description for our analysis. The second was that our experimental system is either thermal or
127 shot noise limited. Since the detection frequency is above 1 MHz, the RIN is small compared
128 with the thermal or shot-noise for the power range that was used. With increasing powers, the
129 photo-detector saturates before RIN dominates the noise over thermal or shot noise (Figure S2d).

130 For the thermal and shot noise contributions, the propagation of the noise from the detector
131 through the LIA is determined by the bandwidth of the filter. A useful expression for the
132 quantification of the noise bandwidth is the noise equivalent power bandwidth (NEPBW, Figure
133 S2a), which assumes a flat (white) noise spectrum. It is modeled as a rectangular-shaped filter,
134 which lets the same amount of noise power pass as the actual filter. The flat noise spectrum
135 assumption is valid for small bandwidths relative to any large non-flatness in the spectrum
136 caused by electronic components (e.g. photo-diode or trans-impedance amplifier). The NEPBW
137 is derived from the discrete time RC filter, and is therefore described by the same TC and n
138 parameters. Integration of the square of the filter transmission (Eq. 3) gives:

$$139 \quad (4) \quad NEPBW = \int_0^{\infty} |H_n(f)|^2 df = \frac{\Gamma(n - \frac{1}{2})}{4\sqrt{\pi} TC \Gamma(n)}$$

140 Where the filter order n is expressed through the gamma function. The NEPBW has frequency
141 units (Hz).

142 **Results**

143 **Calibration of signal and noise**

144 For the calibration of our system we used the Raman signal of a polystyrene (PS) bead as a test
145 sample at 1602 cm^{-1} . The signal calibration coefficient C_{sig} is defined as the product of the

146 Raman cross-section of PS and the number of molecules in the focal volume, propagated through
 147 the collection optics and the detection electronics (photo detector, trans impedance amplifier and
 148 LIA). If we wish to use this result for another analyte than PS, we simply have to determine the
 149 ratio between the signals generated by both analytes on our system (i.e. convert the cross-section
 150 from one to another). Accordingly, C_{TN} , C_{SN} are the thermal and shot noise calibration
 151 coefficients, which are independent of the analyte cross-section in SRS:

152
$$(5) \quad S_{PS} = C_{sig} \cdot P_c P_p$$

153
$$(6) \quad N_T = C_{TN} \cdot \sqrt{NEPBW}$$

154
$$(7) \quad N_S = C_{SN} \cdot \sqrt{P_p \cdot NEPBW}$$

155 where S_{ps} is the signal generated by PS and is measured in Volts at the output of the LIA, P_c is
 156 the average intensity of the modulated carrier and P_p is the intensity of the probe in milli-Watts.
 157 In addition, N_T and N_S are the noise contributions of the thermal noise and the shot noise,
 158 respectively, which are given in Volts. The calibration coefficients were extracted from a fit to
 159 the measurements shown in Figure S2c for the signal and S2d for the noise contributions. In
 160 these measurements the ratio between the carrier and the probe power was always set to 2:1¹⁶,
 161 which is reflected in the slope of 2 in the signal graph (Figure S2c) that it follows from the
 162 product of the carrier and probe powers. From the linear part of that slope we extract the
 163 coefficient C_{sig} following equation (5). The slope of the shot noise region in the noise graph as a
 164 function of probe power in Figure S2d follows a square root relation to the probe power, and is
 165 an indication that the system is indeed shot noise limited when using these powers as explained
 166 in Figure S2b. The coefficient C_{SN} is derived from the slope of Figure S2d, following equation
 167 (7), and C_{TN} is calculated from equation (6), where N_T is measured with no light on the detector.

168 These coefficients are used as default input to the simulations explained below, but can be
169 changed to fit a simulation of any SRS system:

$$170 \quad C_{\text{sig}}=3 \times 10^{-6} \text{ V/mW}^2, C_{\text{TN}}=1.518 \times 10^{-7} \text{ V}/\sqrt{\text{Hz}} \text{ and } C_{\text{SN}}=1.36 \times 10^{-7} \text{ V}/\sqrt{(\text{mW Hz})}.$$

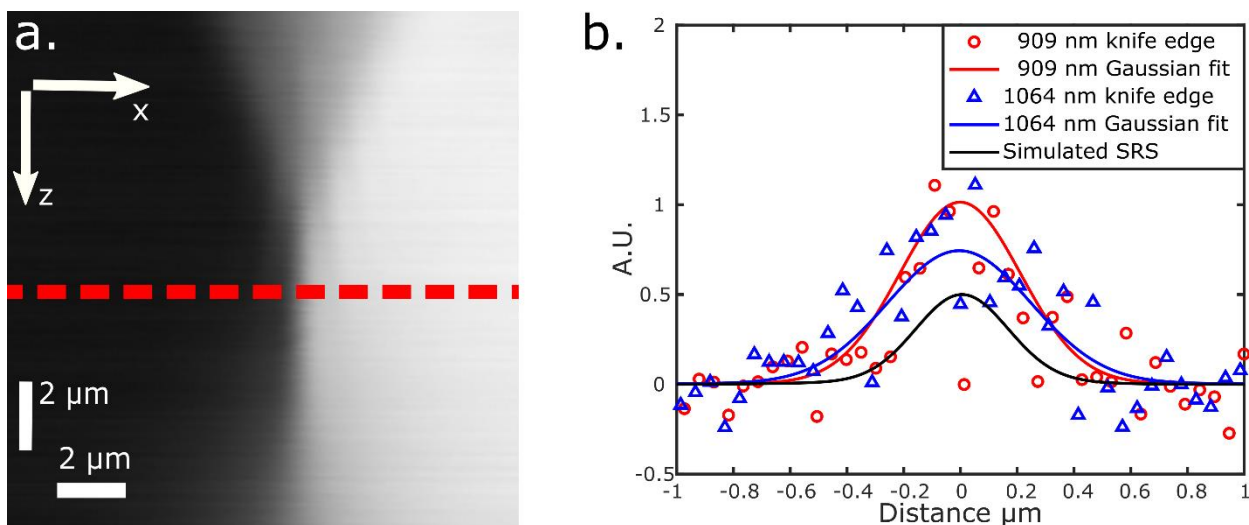
171 **Focal spot size and optical spatial resolution**

172 In order to relate the LIA performance with different settings to imaging parameters of a given
173 object, the focal spot size of SRS has to be considered. Since the SRS signal is the product of
174 two beam intensities, the effective focal spot intensity profile of SRS is the product of the carrier
175 and probe beams' focal spot profiles. Assuming both have a Gaussian intensity profile and are
176 slightly underfilling the objective's back aperture^{17,18}, we can approximate both beams to have a
177 Gaussian profile at the focal plane and their product will be a Gaussian as well. The resulting
178 product beam width or SRS beam full width at $1/e^2$, ω_{SRS} , is described by equation (8)¹⁹:

$$179 \quad (8) \quad \omega_{\text{SRS}} = \frac{\omega_{\text{carrier}} \omega_{\text{probe}}}{\sqrt{\omega_{\text{carrier}}^2 + \omega_{\text{probe}}^2}}$$

180 The focal spot widths of the carrier and the probe beams were measured by a knife-edge
181 measurement, taking the derivative of the intensity profile and fitting it to a Gaussian. Since sub-
182 micron widths were expected, we used a USAF target to replace the knife. This was repeated at
183 various z depths. An X-Z intensity profile of the 1064 nm beam is shown in Figure 1a for
184 illustration (with x being the scanning direction and z as the depth); the dashed red line indicates
185 the depth of the steepest measured intensity profile. The derivative of each line at different
186 depths was fitted to a Gaussian from which the beam widths were extracted. The minimum of
187 these widths was found by fitting a parabola. The effective SRS beam width was determined as
188 described by equation (8). Figure 1b shows the smallest widths from knife edge measurements of

189 the carrier and the probe with a Gaussian fit. The resulting $1/e^2$ width is $0.89 \mu\text{m}$ for the probe
 190 focal spot size and $1.03 \mu\text{m}$ for the carrier focal spot size. Accordingly, the SRS beam effective
 191 spot size width is $0.67 \mu\text{m}$. Following the resolution derivation for a Gaussian beam
 192 approximation as described in the supplementary information (Eq. S2-S4)²⁰⁻²² we get the SRS
 193 Rayleigh resolution as $1.03 \cdot \omega_{\text{SRS}} = 0.69 \mu\text{m}$.



194
 195 Figure 1: A measured beam profile at 1064 nm is shown in (a) to illustrate the result of one
 196 beam knife edge measurement in the lateral and the axial (depth) directions indicated by x and
 197 z, respectively. The dashed red line indicates the steepest slope, i.e. the focal plane depth.
 198 Derivatives of the measured data of the beam profiles at the focal plane are shown in (b) for
 199 the probe at 909 nm (red line) and the carrier at 1064 nm (blue line). Multiplying the fitted
 200 Gaussians of the two beams gives the SRS profile also shown in (b) (black line). Note: 1. One
 201 fourth of the data points are plotted for clarity. 2. SRS beam profile not to scale on the y-axis.

202 **Optimal settings simulation**

203 The optimal settings simulation gives the LIA's filter order and time constant optimal values.
204 In order to properly simulate the SRS imaging behavior, we have to consider first the physical
205 input parameters of the imaging system. The input signal is given by equation (5), and only
206 requires the laser powers as input, given that C_{sig} is calibrated. Upon calibration of C_{TN} and C_{SN} ,
207 the noise contributions can be simulated as well for each TC and filter order with equation (6)
208 and (7) and the NEPBW expression in equation (4). For the optical point spread function (PSF),
209 the required input is the $1/e^2$ radius of the probe and carrier beams and equation (8). A detailed
210 description of the input parameters and the setup parameters is given in Figure S3.

211 Simulation of the lock-in parameters is done with respect to an object size input. The object is
212 modelled as a top-hat (black lines in Figure 2) with a width of the object size and a height of the
213 signal S_{PS} (Eq. 5). First, it is convolved with the PSF (blue lines in Figure 2), which we derived
214 from the SRS signal effective spot size. Then, using the convolution of the input object with the
215 PSF, the input signal in discrete time steps is determined by equation (1) (red line Figure 2). The
216 signal propagation in time translates into a spatial signal propagation by the scanning speed,
217 which is simply the pixel size divided by the pixel dwell time.

218 The LIA parameters are then optimized by running this simulation multiple times over a range
219 of TCs and filter orders, optimizing for either imaging time (for a given CNR), or CNR (for a
220 given imaging time). The CNR⁹⁻¹¹ is calculated as follows:

$$221 \quad (9) \quad CNR = \frac{I_{peak} - I_{valley}}{\sqrt{2} \sqrt{N_T^2 + N_S^2}}$$

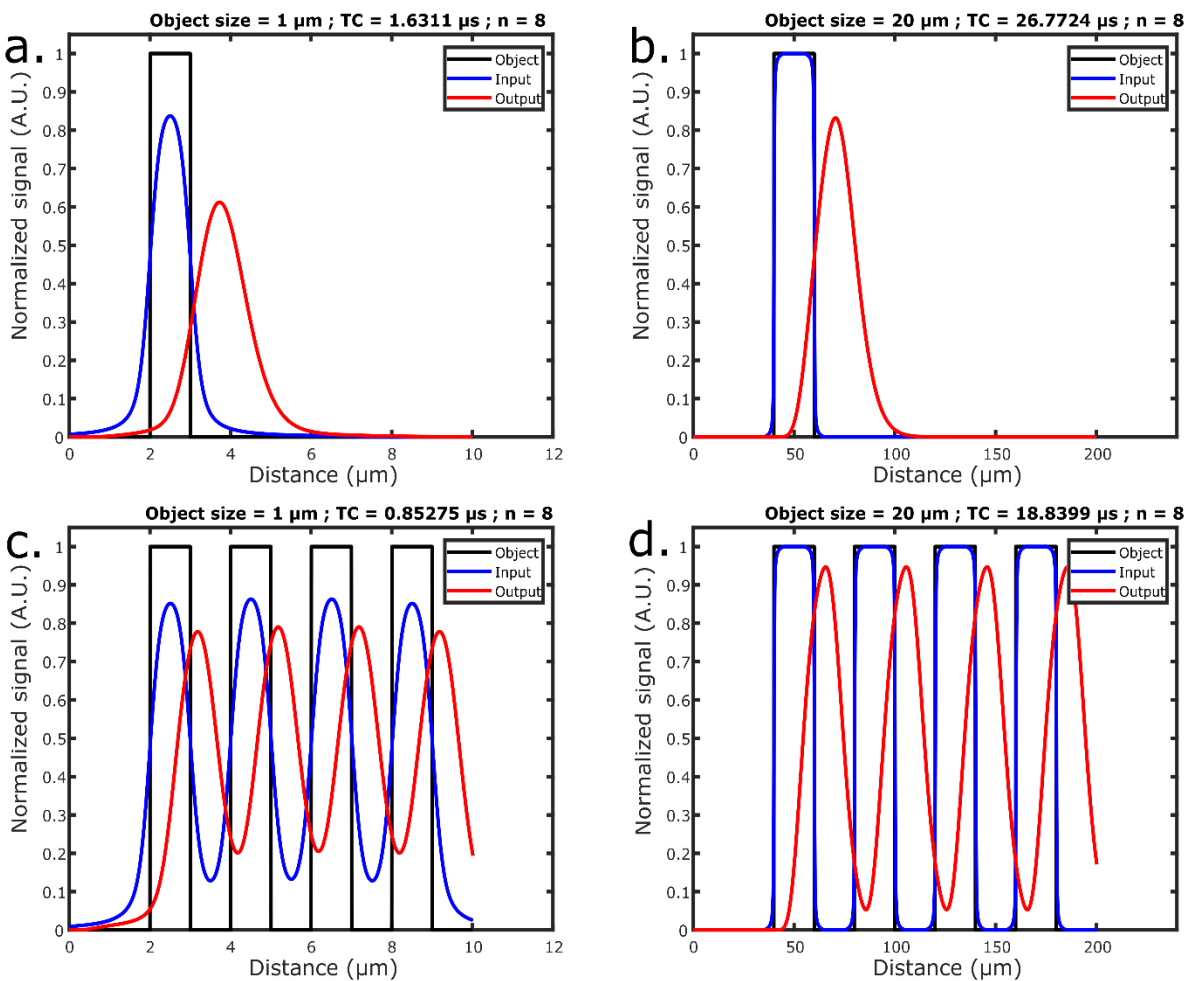
222 where I_{peak} is the signal value at the apex of the output curve, and I_{valley} is the value at a local
223 minimum between two apexes in a dense sample case (red lines in Figures 2c-d). In the sparse
224 sample case, the I_{valley} is zero (red lines in Figures 2a-b). The noise, however, is the same
225 everywhere in SRS, as it is independent of the signal, but rather depends on the probe laser
226 power as illustrated in Figure S2b. The CNR is the difference between two signals with a similar
227 noise level, so there is an additional $\sqrt{2}$ factor in the dominator compared with the SNR, which is
228 simply dividing the signal by the noise. In both cases, CNR is a single term giving a description
229 of the quality of the signal (like SNR¹⁵) as well as a measure to distinguish an object from its
230 surrounding (like contrast).

231 Different lock-in parameters are tested to find the combination that yields the shortest imaging
232 time or the maximum CNR, respectively. This can be done either for a sparse sample (single
233 particle) case or a dense sample case (tightly packed particles). In a dense sample, the object size
234 represents both an object size and the gap between two objects, i.e. the spatial resolution is half
235 of the object's reciprocal (in units of line-pairs per millimeters).

236 The simulation produces plots (Figure 2) to illustrate the signal propagation of a given object in
237 terms of signal response and delay. The LIA setting filter order and TC are in the title of these
238 plots. The full output parameters, like the CNR, filter order, time constant and PDT are then
239 shown in the user interface (see Figure S3).

240 As an example, we tested the response for a PDT as short as 10 μs , for an object in a dense
241 sample with 1 μm object size and 1 μm pixel size. In this test case the maximum CNR was 4.6,
242 found for a TC of 0.85 μs and a filter order of $n=8$ (see figure 2c).

243 Alternatively, the simulation can also optimize the lock-in parameters to find the minimum
 244 imaging time for a specified CNR, which is calculated the same way as described above. In this
 245 case, the shortest PDT is chosen for the optimal TC-filter order combination. For the same test
 246 case above, first setting CNR=2, we get PDT = 2.7 μ s, TC=0.23 μ s with filter order n=8 as the
 247 parameters that give the shortest imaging time for a minimum required spatial resolution in the
 248 scanning direction.



249
 250 Figure 2: The user interface of the SRS optimal parameters simulation is shown in Figure S3. The
 251 power input was 24.7 mW for the carrier and 14.6 for the probe on the sample, respectively.
 252 Pixel dwell time was set to 10 μ s. A visualization of the signal response through the simulated

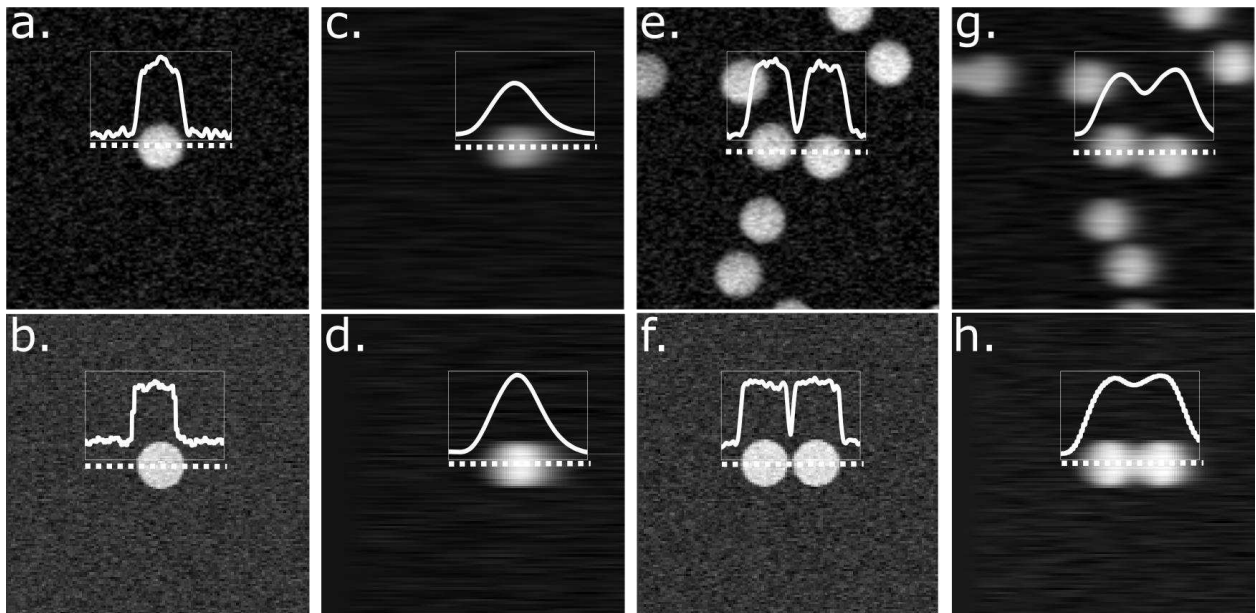
253 system of a CNR optimized case, excluding the noise, is shown in (a) for a single object size of 1
254 μm and in (b) for an object size of 20 μm . In (c) and (d) a simulation is shown for a dense sample
255 with an object size of 1 μm and 20 μm , respectively. The object size represents the half period
256 distance of the spatial modulation, (i.e. it accounts for both the particle and the gap between
257 particles in a dense sample).

258 **Imaging simulation compared with SRS imaging**

259 The same LIA's filter response in equation 1 in combination with the calibrated signal and
260 noise terms (Eq. 5-7) and the PSF (Eq. 9) can be used for visualizing SRS imaging. The imaging
261 simulation receives the aforementioned system and imaging parameters as input together with an
262 one-dimensional or two-dimensional object input. The result is a simulated image of an object
263 passing through the SRS imaging system. Possible input objects are one dimensional top hat
264 object, one dimensional square wave, and two-dimensional round objects to simulate beads. For
265 example, beads imaged with SRS are compared with simulated 2D beads images in Figure 3,
266 both with the same system and imaging parameters.

267 The imaging simulation creates an image using the input objects and input parameters as
268 follows. Firstly, the shape of the object is convolved with the PSF. Secondly, the object is scaled
269 by the beam powers according to equation (5) to form the input signal and the noise is added
270 (Eq. 6 and 7). Finally, the object is passing through the low-pass filter as described by equation
271 (1) by virtual horizontal scanning (left to right). A description of the imaging simulation
272 interface, with different input parameters and setup options, is given in the Supplementary
273 Material, Figure S5.

274 The results in Figure 3 demonstrate the principles discussed in the ‘Optimal setting simulation’
 275 section. Figures 3a and 3b show images from measurements and simulation of a 20- μm bead,
 276 respectively, optimized for a single object size of 1 μm , with a good spatial resolution and high
 277 noise as shown by the profile insets. Doing the same in Figures 3c and 3d with an optimization
 278 for 20 μm objects reduces the noise due to the slower response of the filter (with a narrower filter
 279 bandwidth), but also reduces the signal’s peak height in the measured bead image. The
 280 simulation automatically scales the signal to cover the whole dynamic range. Nevertheless, both
 281 in measurement and simulation, optimization for 20 μm results in a better CNR, which allows us
 282 to detect this single object better in an image with a given PDT, albeit blurred. The resulting
 283 CNR values, together with the optimized lock-in parameters are listed in Table 1. Additionally,
 284 the slower filter response leads to a noticeable horizontal displacement of the objects, as seen in
 285 Figures 3c and 3d compared with Figures 3a and 3b.



286
 287 Figure 3: Imaged and simulated beads with intensity line profiles of 60 μm in the insets. The top
 288 row are 20 μm beads imaged with carrier and probe powers of 24.7 mW and 14.6 mW,

289 respectively. The lock-in settings were optimized for an object size with the optimal settings
 290 simulation: (a) for 1 μm , (c) for 20 μm , (e) for 2 μm , (g) for 20 μm . The bottom row (b, d, f and
 291 h, respectively) are beads simulated with the same parameters and applied powers. The four
 292 left-hand side images (a, b, c and d) are imaged and simulated with the single object criteria,
 293 and the right-hand side (e, f, g and h) for the tightly packed sample criteria.

294 Table 1: comparison of CNR values of images in Fig. 3 that were imaged and simulated with
 295 settings obtained from optimal setting simulation.

CNR values	single 1 μm object; TC=1.6 μs ; n=8	single 20 μm object; TC=26.5 μs ; n=8	dense sample 2 μm ; TC= 1.8 μs ; n=8	dense sample 20 μm ; TC=18.7 μs ; n=8
Imaged:	9.3	20.7	9.0	6.3
Simulated:	7.3	25.4	8.1	5.4

296

297 Figures 3e-h show images of 2 measurement–simulation-pairs of two beads separated by 2 μm .
 298 One pair was optimized for a 2 μm object in a dense sample (Fig. 3e and 3f), and the other for a
 299 20 μm object (Fig, 3g and 3h). In the latter case, the slower filter response leads to a lower noise
 300 level, but also to a less deep signal in the gap between the beads, which counteracts any
 301 improvement of the noise level. Thus effectively, the CNR decreases (see Table 1).

302 **Multiplex SRS imaging simulation**

303 The imaging simulation was generalized to provide not only a visualization of a narrowband
 304 imaging system, but also multiplexed SRS imaging approaches. In this section, we simulated and
 305 investigated settings for a multiplex SRS system, with modulation encoded channels and a single
 306 detector. This analysis of frequency encoded multiplex SRS also considered the channels'

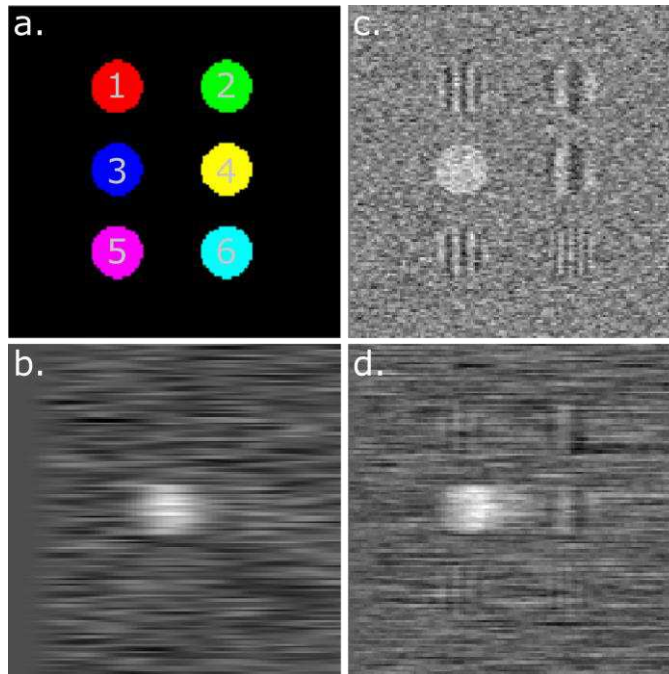
307 spacing, i.e. the separation between adjacent channels in the frequency domain. This is done in
308 order to avoid crosstalk on a limited detection bandwidth while still optimizing for CNR or
309 acquisition speed.

310 We use the same imaging simulation described in the previous section to investigate an
311 imaging approach for the detection of multiple bands at the same time. It is a frequency-encoded
312 multiplex SRS approach, similar to the work done by Liao et al. in 2015⁷. Here we name it
313 ‘single carrier modulation’. In this approach, a combination of a narrowband and a broadband
314 laser beam is used, where the narrowband is used as a probe. The broadband beam is divided into
315 different spectral bands. Each band, that we also call channel, is being modulated at a different
316 frequency. As a result, this multiplex SRS approach has many carriers, while only one probe is
317 used. After the sample, the modulation is transferred to the probe by the SRS process. The probe
318 is then measured by a single detector. Other multiplexing options are shown in the user interface
319 (Figure S5).

320 In multiplex SRS, the low pass filter bandwidth plays a role not only in determining the signal
321 and noise propagation, but also for the crosstalk between the channels. In our experimental setup
322 we used a trans-impedance amplifier to amplify the signal around the modulation frequency. The
323 trans-impedance amplifier has a bandwidth of 43.5 kHz around 3.63 MHz, with an amplification
324 of above 99% of the original amplification of 86 dB. This means that the measured calibration
325 coefficients (Eq. 5-7) provide a good approximation that can be used for the multiplex simulation
326 within that bandwidth. In this section we simulated multiple beads at 6 different modulation
327 channels, modeling samples of different materials. For simplicity, all Raman cross-sections were
328 set to that of the 1602 cm^{-1} band of polystyrene. The frequency separation between adjacent
329 channels was 8.7 kHz to fit the 6 channels in the aforementioned bandwidth.

330 In Figure 4, we show the results of simulations with 3 TC settings, for a hypothetical situation
331 of six different beads of 20 μm diameter, where each bead is in a different channel. Fig 4a is a
332 schematic image showing the beads. Figure 4b is a simulated image with settings optimized for a
333 20 μm object (bead #3 in blue in Fig. 4a) in a sparse sample, which results in no crosstalk; note
334 the horizontal displacement due to the slow filter response. Fig. 4c is an image using parameters
335 optimized for 1 μm , which shows a sharper image but also crosstalk in channel 3 from other
336 channels. Fig. 4d shows the results with filter order 1 and time constant 125 μs , which
337 theoretically should result in the same CNR as in 4b, since these settings have the same NEPBW
338 as in 4b. However, due to the less steep filter shape of filter order 1 than filter order 8, there is
339 more crosstalk from neighboring channels.

340 These results can be understood through the filter transmission (Eq. (3)). If a channel's
341 bandwidth is larger than the frequency distance between neighboring channels, the signal from a
342 neighboring channel will appear as an oscillation modulated at the frequency difference of the
343 channels (i.e. beating frequency at Δf). By multiplying the transmission of the channel at Δf ,
344 with the signal strength at the neighboring channel (Eq. 5), we get the value for the amplitude of
345 this crosstalk oscillation.



346

347 Figure 4: Simulation of 6 channels over a band of 43.5 kHz; 8.7 kHz separation between
 348 neighboring channels. The arrangement of six 20 μm diameter simulated beads in six different
 349 channels is shown in (a). A simulated SRS image of a bead with time constant of 26.5 μs and
 350 filter order 8 in channel 3 is shown in (b). In (c) the same channel is simulated with a time
 351 constant of 1.6 μs and filter order 8, showing crosstalk between channel 3 and the rest of the
 352 channels as a modulation that depends on their frequency difference. Channel 3 was also
 353 simulated with a time constant of 125 μs and filter order 1 (d), which results in the same
 354 NEPBW as the parameters used for b. Despite the same NEPBW, there is much more crosstalk
 355 between the different channels due to the filter shape.

356 Discussion

357 In this study, key parameters of the lock-in amplifier were investigated with respect to imaging
 358 parameters of SRS. We showed that the imaging parameters, like the effective SRS focal spot

359 and laser powers, are important in the analysis for finding the optimal LIA parameters; filter
360 order and time constant. For this analysis, the specific signal and noise propagation through the
361 LIA's low pass filter are explained and described through the calibration coefficients. Based on
362 the imaging parameters and Eq. 1, together with the definition for the NEPBW, we constructed a
363 simulation program to find the optimal lock-in amplifier parameters. The optimization can be
364 done for CNR or imaging speed, and for a sparse sample or a tightly packed sample. We also
365 show an imaging simulation which is able to further evaluate our result. Finally, we showed how
366 the insights we gained on the optimal setting can help to simulate and evaluate more advanced
367 set-ups, such as multiplex SRS.

368 Combining the LIA parameters, the PDT and the SRS beam size (Eq. 8) with the object size to
369 determine the CNR in sparse and dense samples shows the benefit of the optimal setting
370 simulation. The CNR determines with what contrast an object can be imaged with respect to the
371 noise, and with what contrast two objects of a given size can be discerned from one another. This
372 defines the system resolution in terms of contrast. Therefore, we choose CNR as the image
373 quality definition to account for both contrast and noise, which is different from the common use
374 of SNR for image quality assessment¹⁵. The numerical simulation for the signal response in time
375 due to the filter shape is necessary for optimization since signal, contrast and noise are all
376 affected when the LIA parameters are changed and they are constrained by the scanning speed.
377 This is even more so when the CNR is calculated for a tightly packed sample to evaluate the
378 resolution, when also the signal level between objects has to be determined.

379 These principles are illustrated in Figures 2 and 3. In Figure 2, the LIA parameters for CNR
380 optimization are plotted in the title of the graphs in which the signal propagation is shown. The
381 same can be done for acquisition speed optimization. The optimization is done for the smallest

382 object size one would like to observe in a sample. The term “object” here can refer to a particle
383 in a sparse sample, or the half period of the highest spatial frequency in a detailed sample. We
384 demonstrated these principles in Figure 3 by using the result parameters of the optimal settings
385 simulation for (real) imaging and the imaging simulation for comparison. The results of
386 experiment and simulation match quite well, supporting the argument that for an optimized
387 quality of the images, the object size and the nature of the sample have to be considered when
388 imaging with SRS.

389 We also use the imaging simulation to provide insight into a frequency encoded multiplex
390 setup. Different realizations of setups can be investigated, and we demonstrated this for one of
391 them. Figure 4 illustrates how in multiplex SRS the choice of filter bandwidth affects not only
392 the signal time response and the noise levels, but also the crosstalk between the different
393 channels. Although the NEPBW is used here as an expression for the bandwidth, it is not
394 describing the real low pass filter shape which has a shape determined by the filter order.
395 Generally, a steeper slope of the filter’s frequency cutoff is preferred, as shallow slope
396 contributes to crosstalk from other channels (see Figure 4d).

397 Some assumptions, made for this simulation, need to be considered. First, the calibration of the
398 noise assumes a flat spectrum, which is valid for a narrow bandwidth of the low-pass filter
399 compared to any variations in the input frequency spectrum to the LIA, i.e. a trans-impedance
400 amplifier with an amplification band wider than the low-pass filter band. This means that for
401 large bandwidths (very short time constants) the noise propagation cannot be calculated in the
402 way presented in this study. Second, the input object was taken as a top-hat shaped object, which
403 is an unrealistic object shape, especially for micron size objects. For a more realistic shape such
404 as a sphere, the effective signal response will be slower, because it takes longer for the focal

405 volume to completely overlap with the sample. Third, the laser beams are approximated to have
406 a Gaussian profile at the focus, which assumes Gaussian beams before entering the objective
407 (TEM 00), and an under-filling of the objective's back aperture. Of course, under-filling of the
408 objective might reduce the effective numerical aperture, so we recommend matching the $1/e^2$
409 radius of a beam to the objective's back aperture radius at this location. Modelling with Bessel
410 beams should give even more exact solutions to the beam profile especially in the case of
411 overfilled objective's back aperture²³. Fourth, we used a PS bead as our test sample. Commercial
412 PS beads are consistent in size and their physicochemical properties, hence the signal response is
413 expected to be consistent. For correctly simulating another type of object with a significantly
414 different Raman cross-section, one should carefully calibrate for this material, or compare
415 between the PS Raman cross-section and that of the compound, since the SRS spectral response
416 follows the spontaneous Raman spectra^{1,2,24}. Finally, we found that the LIA operating at high
417 frequencies and short time constants is different from the theory prediction (Supplementary Fig.
418 S1). For every LIA these limits should be found to define where the simulation results are valid.
419 Nevertheless, we believe that having a tool which provides these optimal settings can improve an
420 imaging session in a straightforward manner for a given sample and a properly defined setup. For
421 example, such a tool may contribute towards a more accurate analysis of environmental
422 microplastics²⁵.

423 Finally, the imaging simulation was also used to determine crosstalk in a complex setup where
424 a few channels were demodulated simultaneously. By doing this, we showed that many scenarios
425 can be evaluated by using this kind of simulation and analysis. We believe that with the same
426 analysis, other types of setups can be evaluated, prior to their realization. The design process of
427 such a setup can then be made more efficient.

428 **Conclusion**

429 In this study we presented two SRS simulations. One can directly improve SRS imaging by
430 finding optimal LIA parameters of an existing setup for different imaging scenarios. The other
431 simulation provides visualization of SRS imaging results and can also simulate various multiplex
432 SRS approaches (Figure S4).

433 The simulations describe the standard tools used for SRS imaging, i.e. two laser beams,
434 modulator, scanning laser microscope and a lock-in amplifier. Thus, these simulations can be
435 used to facilitate SRS studies, by directly improving SRS imaging, which will be especially
436 important in the use of dynamic or irreplaceable samples. The same approach can also help to
437 design new SRS setups.

438 **Experimental set-up description**

439 The narrow-band stimulated Raman loss setup used here was described previously^{16,19,25,26}. A
440 frequency doubled Nd:YAG laser (Plecter Duo, Lumera) with 80 MHz repetition rate, 8 ps pulse
441 length at a 532 nm output pumped an optical parametric oscillator (OPO, Levante Emerald,
442 APE). A second output laser beam at 1064 nm was amplitude modulated with an acousto-optical
443 modulator (AOM, 3080194, Crystal Technology) at 3.636 MHz. The laser and OPO beams were
444 overlapped temporally with a delay stage and overlapped spatially with a dichroic mirror. The
445 overlapping beams were sent into a laser scanning microscope, 7MP (Zeiss), with a 32× water
446 immersion objective (C-achroplan W, numerical aperture [NA] = 0.85) to scan the sample. All
447 measurements were done with 14.6 mW average power of the probe, and 24.7 mW power of the
448 carrier on the sample.

449 Collection was done by a water immersion condenser (NA = 1.2) below the sample, followed
450 by an optical filter to block the carrier. The probe was detected by a large-area photodetector
451 (DET36A, Thorlabs) integrated with a home-built trans-impedance amplifier, with a resonance
452 amplification at 3.64 MHz and a bandwidth (FWHM) of 0.387 MHz. The large area detector was
453 a requirement stemming from the non-descanned detection of the microscope, and the
454 modulation frequency was a compromise between the detector's (area dependent) capacitance
455 and the trans-impedance amplification.

456 The lock-in amplifier (LIA, HF2LI, Zurich Instruments) was used for signal demodulation, and
457 reading its output is possible in two different ways. One is by directly sending one sample per
458 pixel to the computer with the LIA software (LabOne) which we call digital sampling. The other
459 method is called analog sampling, which sends the samples through an analog output to an
460 analog-to-digital converter (ADC) which integrates all samples per pixel. Only the in-phase
461 component with the carrier is measured. Throughout this study the LIA output was measured
462 using the latter method. Digital acquisition can also be simulated, and it only differs in the
463 calibration coefficients of the noise (see Figure S2d).

464 The simulations and apps were written in Matlab 2018b, including the communication toolbox.
465 The integration in equation 4 was done with Mathematica.

466 **List of abbreviations:**

467 SRS - Stimulated Raman scattering microscopy

468 LIA - lock-in amplifier

469 RIN - relative intensity noise

470 TC - time constant
471 n – filter order
472 SNR - signal to noise ratio
473 CNR - contrast to noise ratio
474 PDT - pixel dwell time
475 NEPBW - noise equivalent power bandwidth
476 PS - polystyrene
477 PSF - point spread function
478 OPO - optical parametric oscillator
479 ADC - analog-to-digital converter

480 **Additional information:**

481 Supporting information for this study can be found in the supplementary information
482 document. It includes: Lock-in behavior characterization, Rayleigh resolution of SRS, Noise
483 behavior, Optimal settings simulation graphical user interface description, Optimal setting
484 algorithm description and Imaging simulation graphical user interface.

485 **References:**

486 1. Cheng J-X, Xie XS: *Coherent Raman Scattering Microscopy*. CRC Press; (2013).
487 doi:10.1201/b12907

- 488 2. Christian W. Freudiger, Min W, Saar BG, et al.: Label-Free Biomedical Imaging with.
489 Science. 322,1857-1861(2008). doi:10.1126/science.1165758
- 490 3. Ozeki Y, Dake F, Kajiyama S, Fukui K, Itoh K: Analysis and experimental assessment
491 of the sensitivity of stimulated Raman scattering microscopy. Opt Express.
492 17,3651(2009). doi:10.1364/oe.17.003651
- 493 4. Nandakumar P, Kovalev A, Volkmer A: Vibrational imaging Based on stimulated
494 Raman scattering microscopy. New J Phys. 11,(2009). doi:10.1088/1367-
495 2630/11/3/033026
- 496 5. Slipchenko MN, Oglesbee RA, Zhang D, Wu W, Cheng JX: Heterodyne detected
497 nonlinear optical imaging in a lock-in free manner. J Biophotonics. 5,801-807(2012).
498 doi:10.1002/jbio.201200005
- 499 6. Saar BG, Freudiger CW, Reichman J, Stanley CM, Holtom GR, Xie XS: Video-rate
500 molecular imaging in vivo with stimulated Raman scattering. Science. 330,1368-
501 1370(2010). doi:10.1126/science.1197236
- 502 7. Liao CS, Wang P, Wang P, et al.: Optical Microscopy: Spectrometer-free vibrational
503 imaging by retrieving stimulated Raman signal from highly scattered photons. Sci
504 Adv. 1,1-9(2015). doi:10.1126/sciadv.1500738
- 505 8. Ferrara MA, Filograna A, Ranjan R, Corda D, Valente C, Sirleto L: Three-dimensional

- 506 label-free imaging throughout adipocyte differentiation by stimulated Raman
507 microscopy. PLoS One. 14,1-16(2019). doi:10.1371/journal.pone.0216811
- 508 9. Dickerscheid D, Lavalaye J, Romijn L, Habraken J: Contrast-noise-ratio (CNR) analysis
509 and optimisation of breast-specific gamma imaging (BSGI) acquisition protocols.
510 EJNMMI Res. 3,1-9(2013). doi:10.1186/2191-219X-3-21
- 511 10. Welvaert M, Rosseel Y: On the definition of signal-to-noise ratio and contrast-to-
512 noise ratio for fMRI data. PLoS One. 8,(2013). doi:10.1371/journal.pone.0077089
- 513 11. Timischl F: The contrast-to-noise ratio for image quality evaluation in scanning
514 electron microscopy. Scanning. 37,54-62(2015). doi:10.1002/sca.21179
- 515 12. Fu D, Lu FK, Zhang X, et al.: Quantitative chemical imaging with multiplex stimulated
516 Raman scattering microscopy. J Am Chem Soc. 134,3623-3626(2012).
517 doi:10.1021/ja210081h
- 518 13. Liao CS, Slipchenko MN, Wang P, et al.: Microsecond scale vibrational spectroscopic
519 imaging by multiplex stimulated Raman scattering microscopy. Light Sci Appl. 4,1-
520 9(2015). doi:10.1038/lssa.2015.38
- 521 14. *Zurich Instruments Ag; HF2 User Manual.*; (2014).
- 522 15. Audier X, Heuke S, Volz P, Rimke I, Rigneault H: Noise in stimulated Raman scattering

- 523 measurement: From basics to practice. *APL Photonics*. 5,(2020).
524 doi:10.1063/1.5129212
- 525 16. Moester MJ, Ariese F, De Boer JF: Optimized signal-to-noise ratio with shot noise
526 limited detection in stimulated raman scattering microscopy. *J Eur Opt Soc*.
527 10,(2015). doi:10.2971/jeos.2015.15022
- 528 17. Wang K, Liang R, Qiu P: Fluorescence Signal Generation Optimization by Optimal
529 Filling of the High Numerical Aperture Objective Lens for High-Order Deep-Tissue
530 Multiphoton Fluorescence Microscopy. *IEEE Photonics J*. 7,1-8(2015).
531 doi:10.1109/JPHOT.2015.2505145
- 532 18. Hess ST, Webb WW: Focal volume optics and experimental artifacts in confocal
533 fluorescence correlation spectroscopy. *Biophys J*. 83,2300-2317(2002).
534 doi:10.1016/S0006-3495(02)73990-8
- 535 19. Moester MJB, Zada L, Fokker B, Ariese F, de Boer JF: Stimulated Raman scattering
536 microscopy with long wavelengths for improved imaging depth. *J Raman Spectrosc*.
537 50,1321-1328(2019). doi:10.1002/jrs.5494
- 538 20. Thomann D, Rines, Sorger P, Danuser G: Automatic fluorescent tag detection in 3D
539 with super-resolution: application to the. *J Microsc*. 208,49-64(2002).
540 <http://www3.interscience.wiley.com/journal/118942950/abstract>.

- 541 21. Oldenboug R, Inoue S: *Handbook of Optics*. 2nd ed. (Bass M.; Van Stryland EW.;
542 Williams DR.; Wolfe WL.; eds.). McGRAW-HILL , INC.; (1995).
- 543 22. Benninger RKP, Piston DW: Two-photon excitation microscopy for unit 4.11 the
544 study of living cells and tissues. *Curr Protoc Cell Biol*.1-24(2013).
545 doi:10.1002/0471143030.cb0411s59
- 546 23. Wang X, Zhan Y, Liang J, Chen X: Simulation of the stimulated Raman scattering signal
547 generation in scattering media excited by Bessel beams. 27(2019).
548 doi:10.1117/12.2508494
- 549 24. Rigneault H, Berto P: Tutorial: Coherent Raman light matter interaction processes.
550 *APL Photonics*. 3,(2018). doi:10.1063/1.5030335
- 551 25. Zada L, Leslie HA, Vethaak AD, et al.: Fast microplastics identification with stimulated
552 Raman scattering microscopy. *J Raman Spectrosc*. 49,1136-1144(2018).
553 doi:10.1002/jrs.5367
- 554 26. Haasterecht L, Zada L, Schmidt RW, et al.: Label-free stimulated Raman scattering
555 imaging reveals silicone breast implant material in tissue. *J Biophotonics*.1-10(2020).
556 doi:10.1002/jbio.201960197

557 **Declarations:**

558 **Availability of data and materials:** All data generated or analyzed during this study
559 are included in this published article and its supplementary information files. The repository
560 URL is provided: <https://zenodo.org/badge/latestdoi/305491047>
561 DOI:10.5281/zenodo.4108540.

562 **Competing interests:** The authors declares that they have no competing interests.

563 **Funding:** We gratefully acknowledge financial support from the Netherlands
564 Organization for Scientific Research (NWO) in the framework of the Technology Area
565 COAST of the Fund New Chemical Innovations (Project “IMPACT”: 053.21.112), and
566 NWO Groot grant to J. F. d. B., and from Laserlab Europe (EU Horizon 2020 program,
567 Grant 654148).

568 **Authors' contributions:** L.Z. conceived the research, L.Z. and B.F. designed the
569 experiments, B.F. programmed the simulation code and characterized the setup, L.Z. edited
570 the simulation code, measured the experimental data and analyzed the data, J.F.D.B and
571 F.A. advised and supervised the research, L.Z. wrote the manuscript with critical revision of
572 H.A.L, A.D.V, J.F.D.B and F.A.

573 **Acknowledgments:** We thank Dr. Benjamin Lochocki for his insightful comments.

574 **Authors' information:** not applicable

575 **Software:**

576 Project name: SRS-simulation

577 Project home page: <https://zenodo.org/record/4108541#.X461s9BvbIU>

578 Archived version: DOI 10.5281/zenodo.4108541

579 Operating system(s): Window10

580 Programming language: Matlab 2018b

581 Other requirements: Matlab communication toolbox.

582 License: MIT License.

583 Any restrictions to use by non-academics: None.

584

585

586

Figures

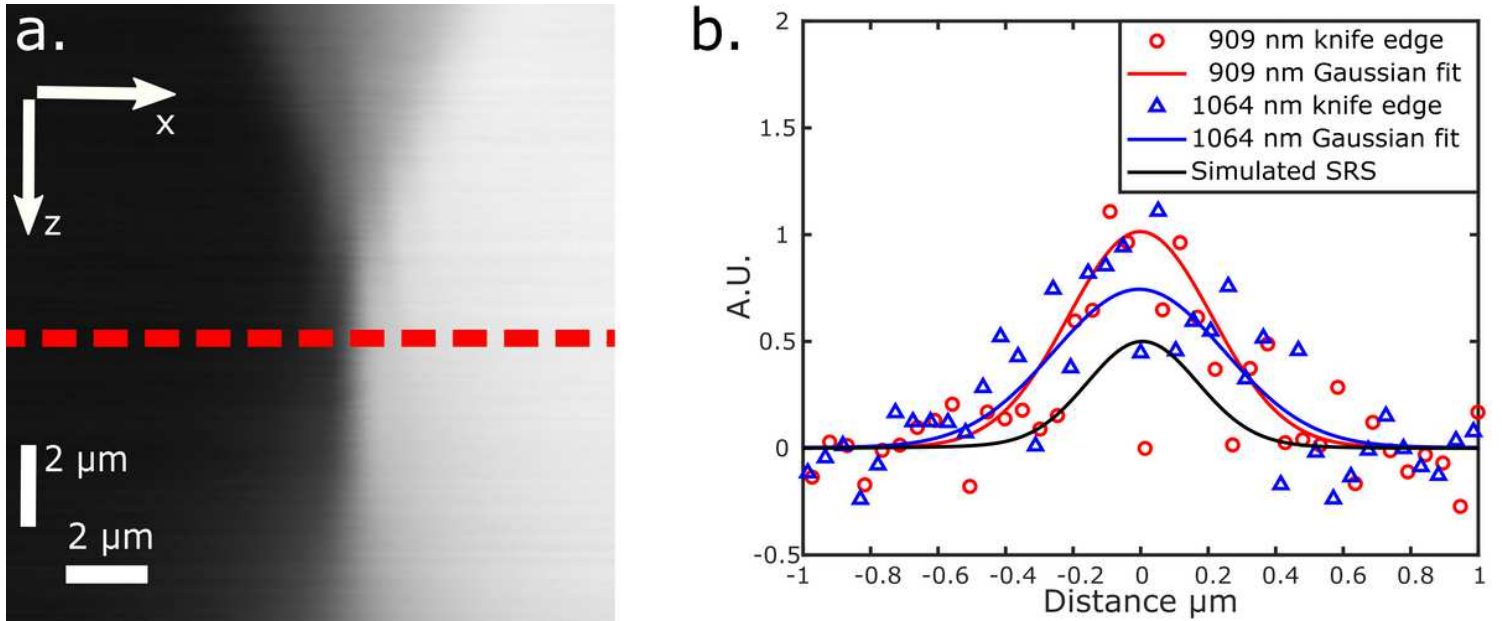


Figure 1

A measured beam profile at 1064 nm is shown in (a) to illustrate the result of one beam knife edge measurement in the lateral and the axial (depth) directions indicated by x and z , respectively. The dashed red line indicates the steepest slope, i.e. the focal plane depth. Derivatives of the measured data of the beam profiles at the focal plane are shown in (b) for the probe at 909 nm (red line) and the carrier at 1064 nm (blue line). Multiplying the fitted Gaussians of the two beams gives the SRS profile also shown in (b) (black line). Note: 1. One fourth of the data points are plotted for clarity. 2. SRS beam profile not to scale on the y-axis.

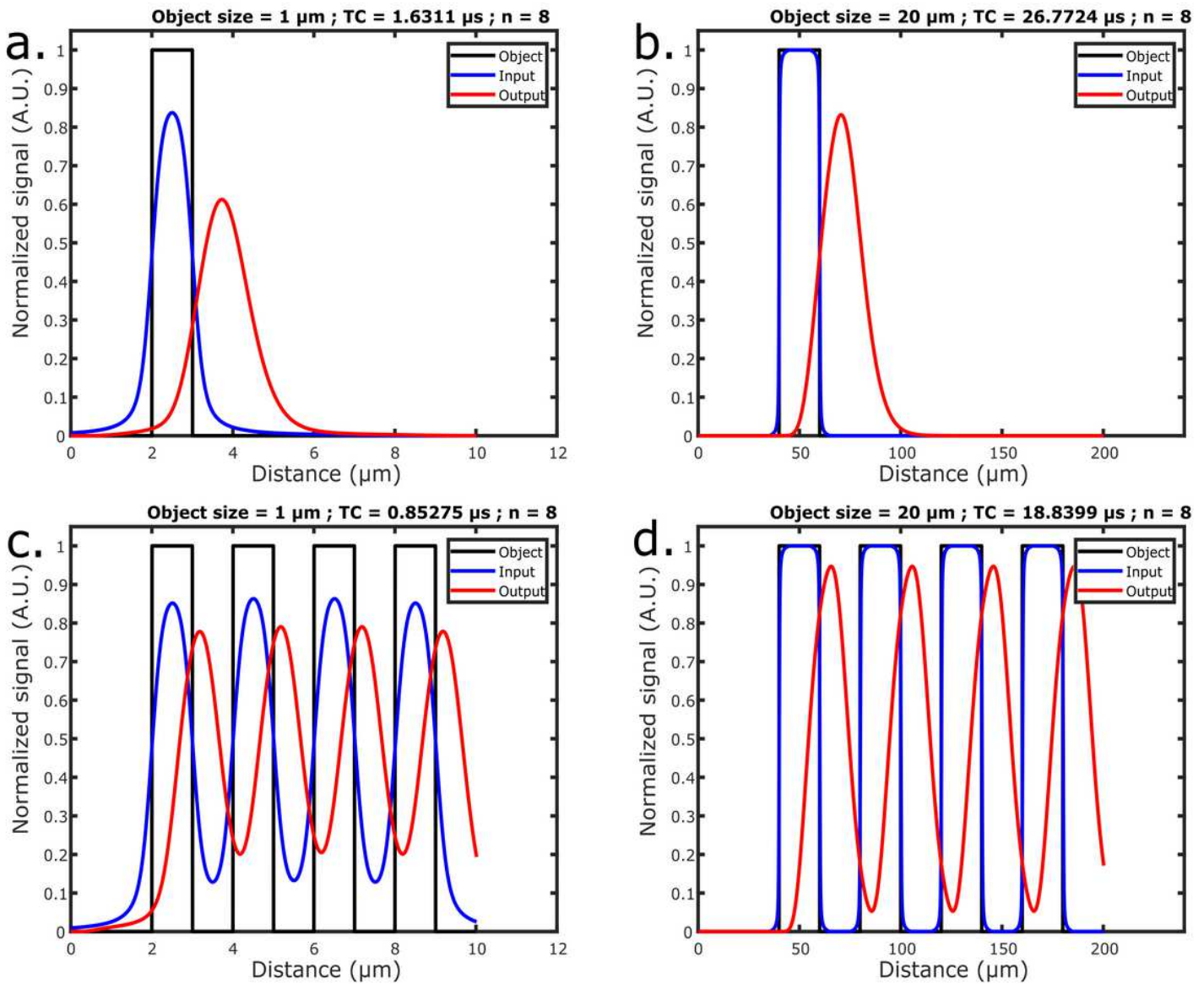


Figure 2

The user interface of the SRS optimal parameters simulation is shown in Figure S3. The power input was 24.7 mW for the carrier and 14.6 for the probe on the sample, respectively. Pixel dwell time was set to 10 μs . A visualization of the signal response through the simulated system of a CNR optimized case, excluding the noise, is shown in (a) for a single object size of 1 μm and in (b) for an object size of 20 μm . In (c) and (d) a simulation is shown for a dense sample with an object size of 1 μm and 20 μm , respectively. The object size represents the half period distance of the spatial modulation, (i.e. it accounts for both the particle and the gap between particles in a dense sample).

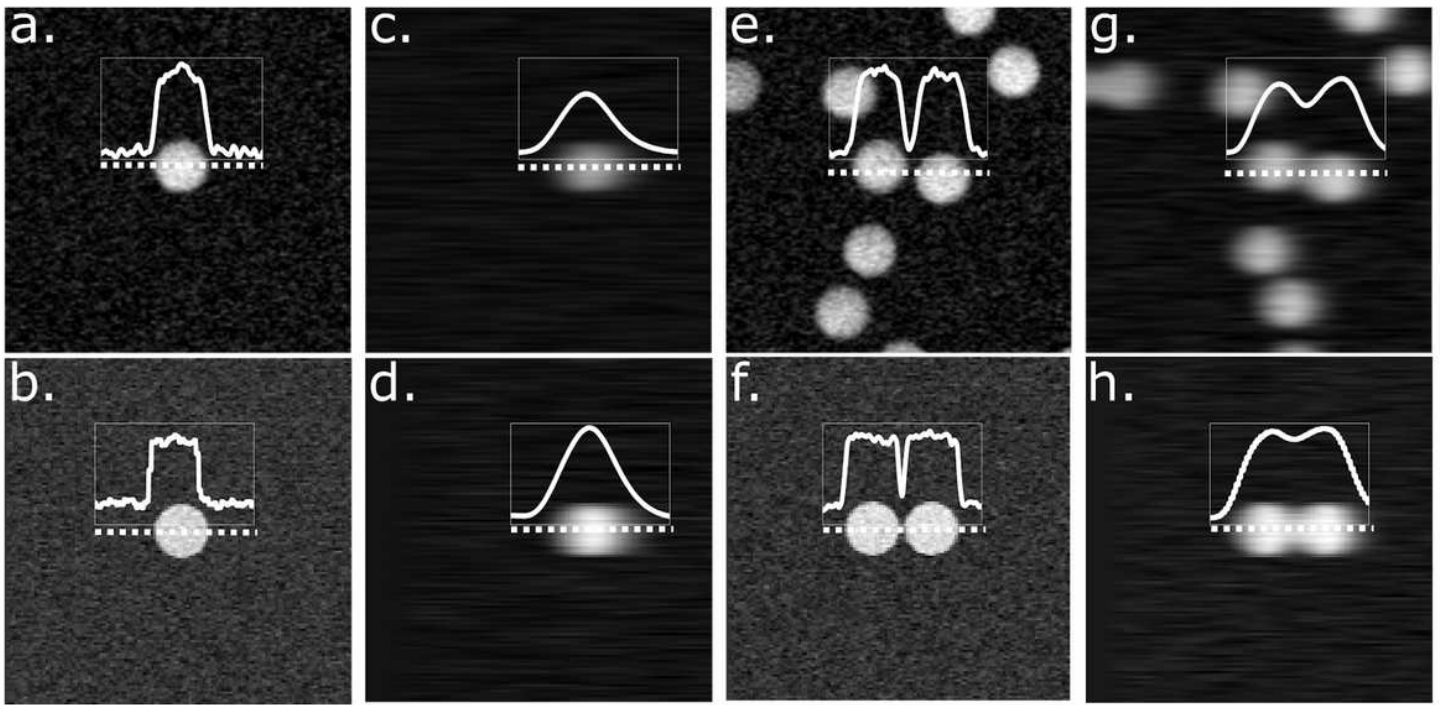


Figure 3

Imaged and simulated beads with intensity line profiles of 60 μm in the insets. The top row are 20 μm beads imaged with carrier and probe powers of 24.7 mW and 14.6 mW, respectively. The lock-in settings were optimized for an object size with the optimal settings simulation: (a) for 1 μm , (c) for 20 μm , (e) for 2 μm , (g) for 20 μm . The bottom row (b, d, f and h, respectively) are beads simulated with the same parameters and applied powers. The four left-hand side images (a, b, c and d) are imaged and simulated with the single object criteria, and the right-hand side (e, f, g and h) for the tightly packed sample criteria.

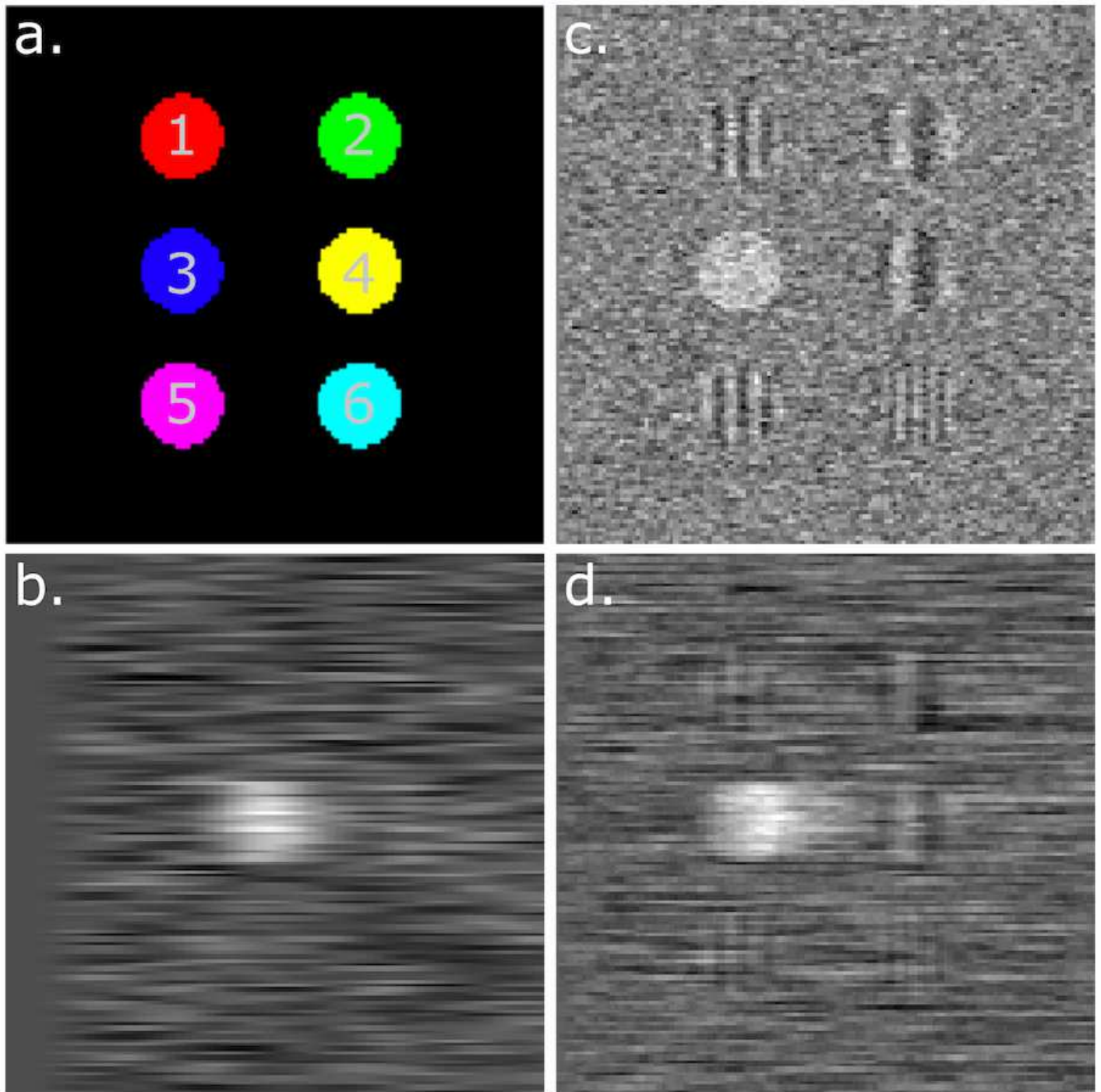


Figure 4

Simulation of 6 channels over a band of 43.5 kHz; 8.7 kHz separation between neighboring channels. The arrangement of six 20 μm diameter simulated beads in six different channels is shown in (a). A simulated SRS image of a bead with time constant of 26.5 μs and filter order 8 in channel 3 is shown in (b). In (c) the same channel is simulated with a time constant of 1.6 μs and filter order 8, showing crosstalk between channel 3 and the rest of the channels as a modulation that depends on their frequency difference. Channel 3 was also simulated with a time constant of 125 μs and filter order 1 (d), which

results in the same NEPBW as the parameters used for b. Despite the same NEPBW, there is much more crosstalk between the different channels due to the filter shape.

Supplementary Files

This is a list of supplementary files associated with this preprint. Click to download.

- [SUPPLEMENTARYsub.1.doc](#)